MIT Open Access Articles

Air entrainment in hairy surfaces

Air entrainment in hairy surfaces

Alice Nasto,[1] Marianne Regli,[1] P.-T. Brun,[2] José Alvarado,[1] Christophe Clanet,[3] and A. E. Hosoi[1,2]

[1]*Department of Mechanical Engineering, Massachusetts Institute of Technology, Cambridge, Massachusetts 02139, USA*

[2]*Department of Mathematics, Massachusetts Institute of Technology, Cambridge, Massachusetts 02139, USA*

[3]*Ladhyx, UMR No. 7646 du CNRS, École Polytechnique, 91128 Palaiseau CEDEX, France*

Motivated by diving semiaquatic mammals, we investigate the mechanism of dynamic air entrainment in hairy surfaces submerged in liquid. Hairy surfaces are cast out of polydimethylsiloxane elastomer and plunged into a fluid bath at different velocities. Experimentally, we find that the amount of air entrained is greater than what is expected for smooth surfaces. Theoretically, we show that the hairy surface can be considered as a porous medium and we describe the air entrainment via a competition between the hydrostatic forcing and the viscous resistance in the pores. A phase diagram that includes data from our experiments and biological data from diving semiaquatic mammals is included to place the model system in a biological context and predict the regime for which the animal is protected by a plastron of air.

I. INTRODUCTION

Hairy surfaces interacting with fluids are ubiquitous throughout nature and play a variety of functional roles. Insects that walk on water use the hair on their legs to trap air and keep afloat [1]; bees [2] and bats [3] use their hairy tongues to entrain viscous nectar while drinking; penguins trap air in their feathers and release it when ascending after dives to reduce drag [4]. In this work, we take inspiration from the fur of semiaquatic mammals, such as that of otters [5,6] and fur seals [7] [shown in Figs. 1(b) and 1(c)]. Compared to species that rely on blubber for insulation, the pelts of semiaquatic mammals that rely on fur for warmth have key morphological differences that contribute to their ability to insulate under water by trapping air. These differences include a greater fur density and the presence of elongated scales on the underhairs [7]. These scales facilitate the interlocking of adjacent hairs, which has been hypothesized to impede penetration of water [5,7]. In polarizing light micrographs of otter fur, air bubbles have been observed to form in these scaly features [5]. Thermographic measurements show the existence of two layers around the body: a warm inner layer that is created by the air trapped in the dense underfur and an external layer made of guard hairs that lie flat and parallel to the body, forming a wet film that protects the underlying fur [6].

To decipher the air entrainment process, we consider a simplified model system of a hair-covered surface plunged into liquid. This geometry echoes model systems of dip coating, as summarized in Fig. 1(a). Previous work is divided into scenarios of withdrawal and plunging. The withdrawal of a smooth plate or a fiber from a bath of fluid is known as Landau-Levich-Derjaguin (LLD) dip coating [8,9]. According to the LLD theory, the thickness h on an untextured surface pulled from a bath is $h \approx 0.94 \ell_c \mathrm{Ca}^{2/3}$, where $\ell_c = (\gamma/\rho g)^{1/2}$ is the capillary length and $\mathrm{Ca} = \mu V/\gamma$ is the capillary number. Here γ is the air-liquid surface tension, ρ is the density of the fluid, g is the acceleration of gravity, μ is the fluid's dynamic viscosity, and V is the withdrawal velocity. For the scenario of plunging a smooth surface into a liquid bath, the contact angle between the liquid and the substrate is known be a function of the capillary number and entrainment of air is observed beyond a critical capillary number [10,11]. When a smooth wet plate is plunged into a bath, the dynamic meniscus is observed to buckle, modifying the shape of the classic LLD meniscus [12].

The addition of microtexture enhances the uptake of fluid compared to LLD dip coating. In particular, micropillar-textured surfaces have been studied in the context of liquid entrainment as
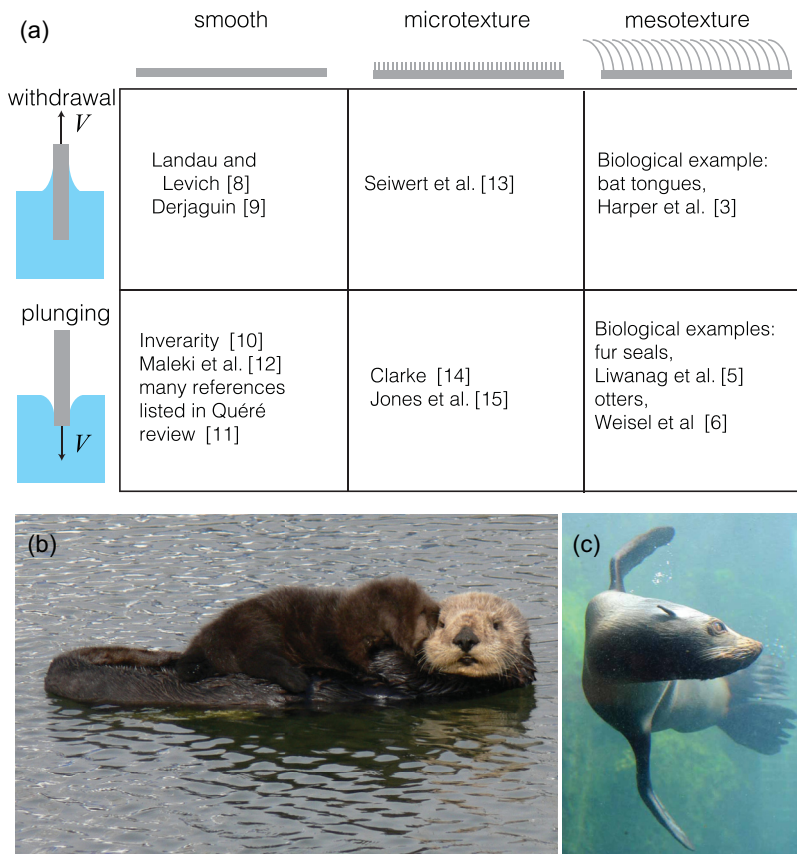
FIG. 1. (a) Sample studies in the literature relevant to dip coating. They are classified by the direction in which the substrate crosses the interface and its texture. (b) Sea otters (photo credit: Jodie Wilson, licensed under CC BY 2.0) (c) Fur seal (photo credit: Ross Elliot, licensed under CC BY 2.0).

they are drawn out of a bath of fluid [13]. The texture thickens the entrained film, which has two layers: a trapped layer contained within the texture of the surface and a free layer that extends beyond it. Unlike classic LLD theory, the shape of the meniscus for a textured plate does not have a universal shape. Experimental studies on plunging rough surfaces in liquid have investigated both dynamic [14] and static scenarios [15] in which the microscale roughness contributes to entrainment of air and resists substrate wetting; however, a general predictive model in these scenarios is lacking.

Though most work on coating of textured surfaces has focused on textures at the microscale, we are interested in textures at the mesoscale, namely, millimeters and centimeters, which is relevant to hair. In this study, we investigate hairy textures plunged in fluid and rationalize the resulting dynamic air entrainment.

II. EXPERIMENTAL SETUP

Hairy surfaces, shown in Fig. 2(a), are cast from polydimethylsiloxane (PDMS) elastomer (with Young's modulus $E = 2$ MPa) using laser cut acrylic molds (see Ref. [16]). The hairs have a length of $L = 2.7$ mm and have a diameter ranging from $e = 0.25$ mm at the tip to $e = 0.35$ mm at the base (we use an average value of $e = 0.3$ mm in the model). The hairs are spaced in a hexagonal arrangement [as shown in Fig. 2(b)], with a center-to-center spacing d ranging across values $d = 0.5, 0.75, 1.0, 1.5, 2$ mm. The edge-to-edge distance between adjacent pillars is
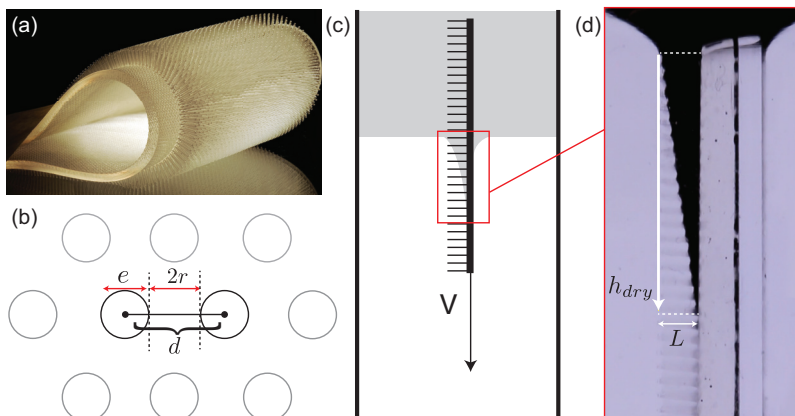
FIG. 2. (a) Photo of a hairy surface cast from PDMS (photo credit: Felice Frankel). (b) Top-view schematic of hairs arranged in a hexagonal pattern. The edge-to-edge distance between adjacent pillars is $2r = d - e$, where e is the pillar's diameter and d the spacing between them. (c) Side-view schematic of the experiment. Hairy surfaces are plunged into fluid at speed V. (d) Representative image from experiments (viscosity $\nu = 10\,000$ cSt, $r = 1$ mm, and $V = 5$ mm/s). Dark regions indicate air; lighter gray regions are fluid: The base plate, supporting the pillars, remains dry above the depth h_{dry}.

$2r = d - e$, as shown in Fig. 2(b). The hairy surfaces are plunged into silicone oil at a speed V using a motorized stage [Figs. 2(c) and 2(d)].

In Fig. 3(a) we show a time-series sequence of snapshots from a typical experiment with $d = 1$ mm and $V = 10$ mm/s. As the sample is plunged, air is entrained and liquid penetrates between the hairs forming a wedge-shaped wetting front that advances the interface between liquid (light) and air (dark) regions. For $t < 1$ s, the wetting front progresses through a series of transient shapes before steady state is attained. For $t \geqslant 1$ s, steady state is reached and the wetting front is stationary in the laboratory frame as the sample continues to plunge into the bath. In this steady state, the imbibition of liquid balances the entrainment of air drawn from above. The wetting front is stable, i.e., no fingering instabilities are observed in the spanwise direction. The steady-state depth to which the air is entrained is denoted by the dry depth h_{dry}, as shown in Fig. 2(d).

Figure 3(b) contains snapshots showing the steady-state entrainment of air for various hair densities and two diving velocities: 15 and 40 mm/s for silicone oil of viscosity $\nu = 1000$ cSt. The depth of entrainment h_{dry} increases with V and decreases with hair spacing d. For a smooth plate with no hairy texture, i.e., the reverse smooth LLD plate plunging scenario shown at the far right in Fig. 3(b), the air entrainment is considerably less than that of the hairy-textured surfaces.

III. MODEL

To model the system, shown in Fig. 4(a), we consider the configuration in which hairs of length L are plunged in liquid at a speed V. The x direction is defined parallel to the hairs and the y direction perpendicular in the laboratory frame. As the hairs are plunged, the liquid penetrates between the hairs, forming a wetting front where the liquid advances. The following geometric parameters are defined in Fig. 4: The depth at which the liquid penetrates to the base of the hairs (at $x = L$) is defined as h_{dry}, the depth of the meniscus that forms at the surface of the liquid bath is denoted by y_m, and the flat liquid-air interface is where $y = 0$ is defined.

We approximate the flow between hairs as flow in a "tube" [17] with radius r, with $2r = d - e$ as defined in the previous section [see Fig. 4(b)]. The four effects at play are viscous dissipation, Laplace pressure, inertia, and hydrostatic pressure. Additionally, owing to the presence of a contact line, we expect a force per unit length resisting the motion of the wetting front and scaling as $\gamma \mathrm{Ca}^{2/3}$
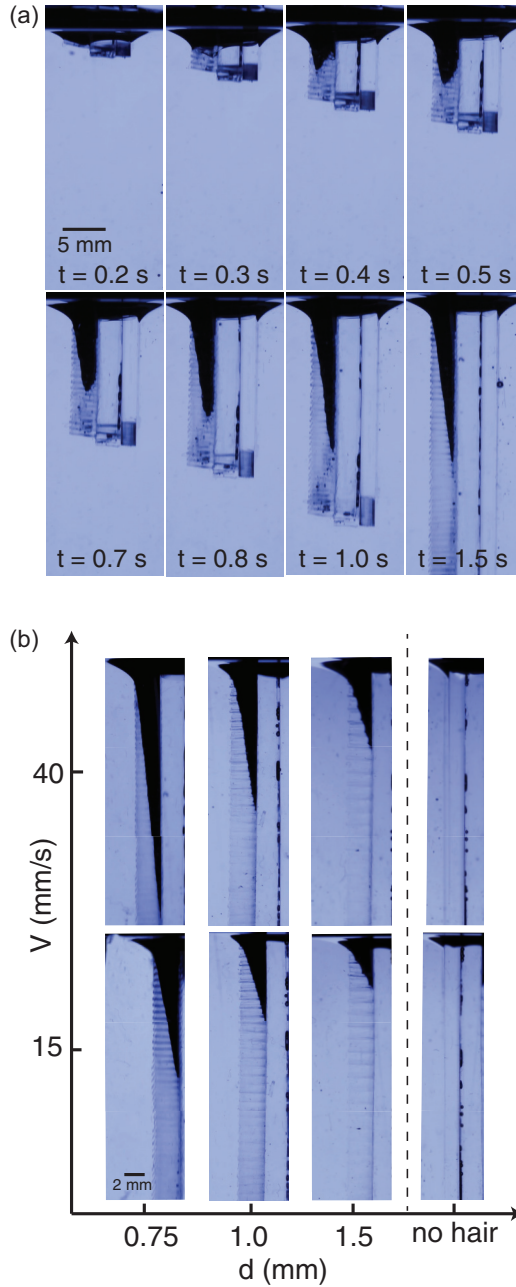
FIG. 3. (a) Time-series snapshots of a sample with hairs of $d = 0.75$ mm plunging into silicone oil with viscosity $v = 1000$ cSt at a rate of 25 mm/s during the transient phase. (b) Snapshots of steady-state wetting profiles for experiments with silicone oil with viscosity $v = 1000$ cSt.

[18], where the capillary number is based on the front speed. In the range of physical parameters explored, we always find this contact line force to be negligible. In the experiments, the hairs were not observed to bend. To confirm that we may neglect bending in our analysis, we model a hair as a cylindrical beam with bending rigidity $B = 10^{-11}$ N m^2 [19] subject to shear stress from the
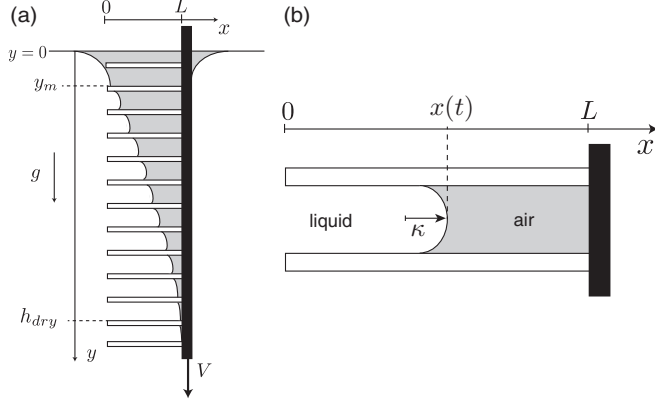
FIG. 4. (a) Schematic of dynamic entrainment showing the coordinate system for the model. Hairs of length L are plunged in liquid at a speed V. The air-liquid interface is positioned at $y = 0$ and h_{dry} denotes the depth at which the air liquid wets the base of the hairs. (b) Schematic of adjacent hairs forming a capillary "tube" of radius r. The meniscus, of curvature κ, has the position $x(t)$ and advances at speed $\dot{x}$.

boundary layer of size $\delta \sim [\nu(L_0 - y)/V]^{1/2} \sim 10^{-2}$ m acting at the tip of the hairs, where ν is the kinematic viscosity and L_0 is the depth to which the sample has been plunged. The tip displacement ϵ is obtained by balancing the bending resistance $B\epsilon/L^3$ and the viscous force $\mu V e^2/\delta$. We find that the tip displacement is on the order of a few percent ($\sim 5\%$) of the radius of a hair, which is consistent with our observation. Hence we proceed assuming rigid hairs.

At steady state, the balance of pressure at the liquid-air interface at a depth y is given by

$$P_0 + \rho g y + \frac{1}{2}\rho \dot{x}^2 - \gamma \kappa - \frac{\mu}{k}\frac{x\dot{x}}{r^2} = P_0, \tag{1}$$

where x and $\dot{x}$ represent the position and speed of the wetting front, respectively, P_0 denotes the ambient pressure, κ is the air-liquid meniscus curvature, and kr^2 is the effective permeability of the hair network [see Fig. 4(b)]. Here the terms on the left correspond to the pressure on the liquid side of the channel and the terms on the right to the air side. Note that the plate speed V does not enter directly into Eq. (1) as we neglect any component of the flow along the plate (in the y direction). Instead, V effectively sets the rate at which the depth y is varied.

To determine which terms dominate, we first balance the Laplace pressure and hydrostatic pressure terms, yielding the characteristic depth ℓ_c^2/r at which capillary and hydrostatic effects are comparable (where $\ell_c = \sqrt{\gamma/\rho g}$ is the capillary length). This characteristic depth is millimetric, so it is exceeded by the depth y at which the samples are plunged by two orders of magnitude. Since $h_{\text{dry}} \gg \ell_c^2/r$, capillary effects are negligible over the bulk of the sample. In addition, the meniscus of the wetting front curves oppositely to what is expected for wetting in a capillary tube, further validating the assumption that surface tension is not a dominating effect. Note that this is not surprising considering that $\text{Ca} = \mu\dot{x}/\gamma \simeq 10^{-1}$, where $\dot{x}$ is the speed of the wetting front, which is sufficiently large for the viscous effects to invert the curvature of the meniscus [20–22], as shown in Fig. 4.

Next we compare the inertial and viscous terms in the pressure balance and denote the Reynolds number by $\text{Re} = kr^2\dot{x}/\nu x$. Initially, when the liquid enters between the hairs, x is arbitrarily small for a very short period of time in which inertial effects dominate. However, for $x \sim r$, the Reynolds number $\text{Re} \simeq 10^{-3}$ is small. Hence, for most of the duration of the experiment, viscous effects dominate. With these two approximations, Eq. (1) reduces to

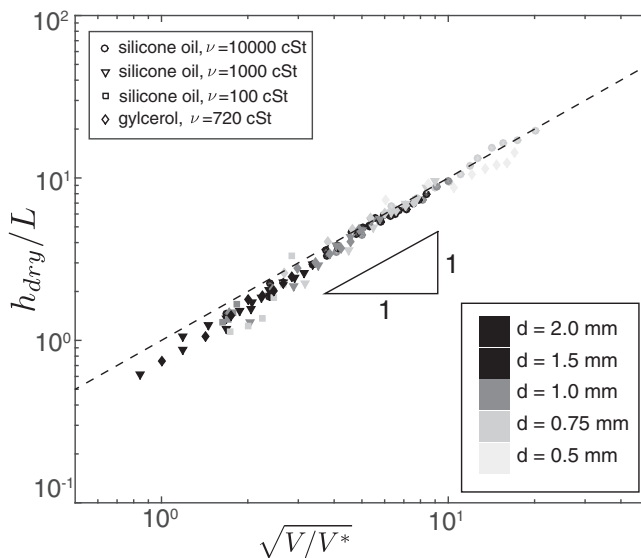$$\rho g y = \frac{\mu}{k}\frac{x\dot{x}}{r^2}. \tag{2}$$

FIG. 5. Experimental values of the dry length h_{dry}/L shown as a function of the diving speed V relative to the characteristic imbibition speed V^*. The darkness of symbols is indicative of spacing, with the lightest to darkest corresponding to increasing spacing with values $d = 0.5, 0.75, 1, 1.5, 2$ mm.

Integrating Eq. (2) using the relation $dy/dt = V$, we obtain the profile of the wetting front

$$x^2 = \frac{V^*}{V}\left(y^2 - y_m^2\right), \tag{3}$$

where $V^* = k\rho g r^2/\mu$ is the characteristic imbibition speed of our problem and y_m is the integration constant defined such that $x(y = y_m) = 0$ [see Fig. 4(a)]. In our system, $y_m \approx \ell_c$, so y_m is small relative to the typical depth at which we operate and thus is neglected in the rest of our analysis. Following this approximation, we find that the front position in steady state is defined by

$$y(x) \simeq \sqrt{V/V^*}x. \tag{4}$$

This shape is the result of the competition between the imposed downward linear motion $y = Vt$ and the invasion of each tube in which the front position is given by $x \sim \sqrt{VV^*}t$. Both processes are linear in time so the equilibrium profile is linear as evident in Fig. 3. In order to quantitatively assess the shape of the air-liquid front, we derive the expression for h_{dry}, the depth at which the wetting front penetrates all the way to the base of the hairs at $x = L$:

$$h_{\mathrm{dry}} = \sqrt{\frac{V}{V^*}}L. \tag{5}$$

IV. DISCUSSION

Using experimental data, we test the prediction for h_{dry} from Eq. (5) by plotting h_{dry}/L as a function of $\sqrt{V/V^*}$ in Fig. 5. The data from experiments with a range of velocities V, hair spacings d, and viscosities μ (spanning three orders of magnitude) collapse onto a single master curve predicted in Eq. (5). Both the slope and the prefactor are recovered. Note that for generating this plot we used $k = 1$ for V^*. This constant value of $k = 1$ validates that the permeability kr^2 scales with the cross-sectional area of the tube [23]. The data include experiments with silicone oil and glycerol, which have significantly different wetting properties with respect to PDMS. Despite this
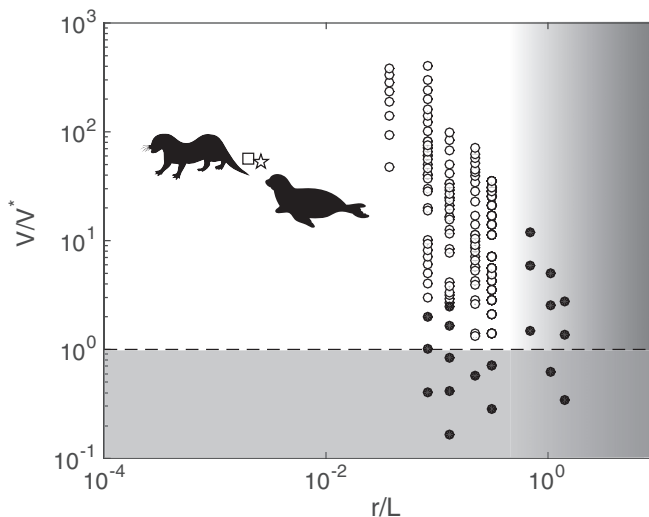
FIG. 6. Phase diagram with points indicating where in parameter space experiments were conducted. Closed symbols indicate experiments where hairy samples were fully wetted and open symbols indicate experiments in which samples entrained air and were only partially wetted. The star and square correspond to physiological data for fur seals [7] and river otters [5], respectively.

difference in wetting properties, the data collapse, further verifying that surface tension is negligible in this scenario.

Figure 6 shows a phase diagram with two dimensionless ratios: the ratio of the spacing r to length L of the hair and the ratio of the diving speed V to the imbibition speed V^*. The points on the phase diagram indicate where experiments have been performed. Open circles denote experiments where entrainment was observed; closed circles denote no entrainment. We specify no air entrainment as cases in which the air entrainment depth does not exceed the spacing between hairs. The gray areas indicate regions where we would not expect air entrainment to occur. The lower horizontal boundary $V/V^* = 1$ results from the competing time scales of the diving speed and the imbibition speed; the diving speed must exceed imbibition speed for air to be entrained. The upper vertical boundary $r/L = 1$ is a geometric requirement for the hairs to be sufficiently long such that a meniscus that bridges two hairs does not touch the base of the hairs, i.e., we are operating in the "long tube limit". Additionally, it is important to note that the model is relevant only for r smaller than the capillary length ℓ_c such that a meniscus can form a bridge between two hairs. Using biological data for fur seals [7] and river otters [5], we add points on the phase diagram corresponding to geometric and dynamic parameters relevant to these animals (star and square, respectively), both of which lie well within the dynamic air entrainment regime. Due to practical limitations of the fabrication techniques used to create the hairy surfaces, we were unable to conduct experiments with the hair spacing and length ratio corresponding to real animals.

While this analysis explains how a furry animal could dynamically entrain air in its fur, we do not yet understand how these animals are able to keep the air trapped in their fur in a static scenario, which could rely on several features of semiaquatic mammalian fur that are not included in our model. Our model has thus far only considered relatively short hairs of uniform length that do not bend significantly. In reality, fur has two lengths of hairs: long deformable guard hairs and short underfur. For long deformable hairs, elastocapillary adhesion may play an important role and could contribute to the formation of the observed wet film in the guard hairs that protects the underlying fur from getting wet [6]. Further work to understand the physical mechanism by which this fur is effective in water could inform the design of performance textiles for wet and cold environments. This approach to modeling hairy surfaces could also be applied to the reverse scenario, to understand

how pulling a hairy textured surface out a liquid can entrain liquid, such as the case for this bat drinking nectar with a hairy tongue [3].

Finally, we note that although this work is inspired by semiaquatic mammals and the practical application of dip coating, we have also uncovered a rationale for a universal interface shape that contributes to a fundamental understanding of the wetting of mesoscale textures and fits into the context of the canonical work on dip coating model systems.

[1] J. W. M. Bush, D. L. Hu, and M. Prakash, The integument of water-walking arthropods: Form and function, Adv. Insect Physiol. **34**, 117 (2007).

[2] W. Kim, T. Gilet, and J. W. M. Bush, Optimal concentrations in nectar feeding, Proc. Natl. Acad. Sci. USA **108**, 16618 (2011).

[3] C. J. Harper, S. M. Swartz, and E. L. Brainerd, Specialized bat tongue is a hemodynamic nectar mop, Proc. Natl. Acad. Sci. USA **110**, 8852 (2013).

[4] J. Davenport, R. N. Hughes, M. Shorten, and P. S. Larsen, Drag reduction by air release promotes fast ascent in jumping emperor penguins—A novel hypothesis, Marine Ecol. Prog. Ser. **430**, 171 (2011).

[5] J. W. Weisel, C. Nagaswami, and R. O. Peterson, River otter hair structure facilitates interlocking to impede penetration of water and allow trapping of air, Can. J. Zool. **83**, 649 (2005).

[6] R. A. Kuhn and W. Meyer, Infrared thermography of the body surface in the Eurasian otter *Lutra lutra* and the giant otter *Pteronura brasiliensis*, Aquat. Biol. **6**, 143 (2009).

[7] H. E. M. Liwanag, A. Berta, D. P. Costa, M. Abney, and T. M. Williams, Morphological and thermal properties of mammalian insulation: The evolution of fur for aquatic living, Biol. J. Linnean Soc. **106**, 926 (2012).

[8] L. Landau and B. Levich, Dragging of a liquid by a moving plate, Acta Physicochim. URSS **17**, 42 (1942).

[9] B. Derjaguin, On the thickness of the liquid film adhering to the walls of a vessel after emptying, Prog. Surf. Sci. **43**, 134 (1993).

[10] G. Inverarity, Dynamic wetting of glass fibre and polymer fibre, British Polymer J. **1**, 245 (1969).

[11] D. Quéré, Fluid coating on a fiber, Annu. Rev. Fluid Mech. **31**, 347 (1999).

[12] M. Maleki, M. Reyssat, F. Restagno, D. Quéré, and C. Clanet, Landau-Levich menisci, J. Colloid Interface Sci. **354**, 359 (2011).

[13] J. Seiwert, C. Clanet, and D. Quéré, Coating of a textured solid, J. Fluid Mech. **669**, 55 (2011).

[14] A. Clarke, Coating on a rough surface, AIChE J. **48**, 2149 (2002).

[15] P. R. Jones, X. Hao, E. R. Cruz-Chu, K. Rykaczewski, K. Nandy, T. M. Schutzius, K. K. Varanasi, C. M. Megaridis, J. H. Walther, P. Koumoutsakos, H. D. Espinosa, and N. A. Patankar, Sustaining dry surfaces under water, Sci. Rep. **5**, 12311 (2015).

[16] See Supplemental Material at http://link.aps.org/supplemental/10.1103/PhysRevFluids.1.033905 for details of sample fabrication, geometry, and mechanical properties.

[17] E. W. Washburn, The dynamics of capillary flow, Phys. Rev. **17**, 273 (1921).

[18] I. Cantat, Liquid meniscus friction on a wet plate: Bubbles, lamellae, and foamsa, Phys. Fluids **25**, 031303 (2013).

[19] The bending rigidity is calculated using $B = Ee^4/12(1 - \nu^2)$, where E is the Young's modulus of the PDMS elastomer and $\nu = 1/2$ is Poisson's ratio.

[20] R. L. Hoffman, A study of the advancing interface. I. Interface shape in liquid-gas systems, J. Colloid Interface Sci. **50**, 228 (1975).

[21] J. Bico and D. Quéré, Falling slugs, J. Colloid Interface Sci. **243**, 262 (2001).

[22] L. H. Tanner, The spreading of silicone oil drops on horizontal surfaces, J. Phys. D **12**, 1473 (1979).

[23] E. Guyon, *Physical Hydrodynamics* (Oxford University Press, Oxford, 2001).